Materials Science & Engineering C 126 (2021) 112104

Contents lists available at ScienceDirect

Materials Science & Engineering C

journal homepage: www.elsevier.com/locate/msec

Sustainable aquaculture side-streams derived hybrid biocomposite for bone tissue engineering

Jun Kit Wang [a], Çiğdem Çimenoğlu [a], Nicole Mein Ji Cheam [a], Xiao Hu [a,b], Chor Yong Tay [a,b,c,d,*]

[a] School of Materials Science and Engineering, Nanyang Technological University Singapore, N4.1, 50 Nanyang Avenue, Singapore 639798, Singapore
[b] Environmental Chemistry and Materials Centre, Nanyang Environment & Water Research Institute, 1 CleanTech Loop, CleanTech One, Singapore 637141, Singapore
[c] School of Biological Sciences, Nanyang Technological University Singapore, 60 Nanyang Drive, Singapore 637551, Singapore
[d] Energy Research Institute, Nanyang Technological University Singapore, 50 Nanyang Drive, Singapore 637553, Singapore

ARTICLE INFO

Keywords:
Waste valorization
Green manufacturing
Collagen
Hydroxyapatite
Bone tissue engineering

ABSTRACT

Despite being a rich source of bioactive compounds, the current exploitation of aquatic biomass is insufficient. Majority of the aquaculture industry side-streams are currently used for low-value purposes such as animal feed or composting material, with low economical returns. To maximize resource reuse and minimize waste generation, valorization efforts should be augmented with the aim to produce high-value products. Herein, we present a novel aquaculture wastes-derived multi-scale osteoconductive hybrid biocomposite that is composed of chemically crosslinked American bullfrog (*Rana catesbeiana*) skin-derived type I tropocollagen nanofibrils (~22.3 nm) network and functionalized with micronized (~1.6 μm) single-phase hydroxyapatite (HA) from discarded snakehead (*Channa micropeltes*) fish scales. The bioengineered construct is biocompatible, highly porous (>90%), and exhibits excellent osteoconductive properties, as indicated by robust adhesion and proliferation of human fetal osteoblastic 1.19 cell line (hFOB 1.19). Furthermore, increased expression level of osteo-related ALPL and BGLAP mRNA transcripts, as well as enhanced osteocalcin immunoreactivity and increasing Alizarin red S staining coverage on the hybrid biocomposite was observed over 21 days of culture. Collectively, the devised "waste-to-resource" platform represents a sustainable waste valorization strategy that is amendable for advanced bone repair and regeneration applications.

1. Introduction

Waste is a huge global issue. Along with the increasing human activities and expanding population, the volume of solid waste generated is expected to reach 2.2 billion tons by 2025 [1]. As such, there are extensive and concerted efforts to pursue sustainable product development and strategies for effective waste management, including electronic [2,3], food [4,5], packaging [6], and also farming wastes [7]. Aquaculture, the cultivation of various types of aquatic fauna (e.g., fish, crustaceans, amphibians, mollusks) and flora (e.g., plants, weeds) under controlled farming conditions, has become an essential source of food to meet the nutritional needs of the rapid global population growth. With an average world production and utilization exceeding 70 million tons per year, aquaculture is one of the fastest-growing food production sectors in recent years [8]. However, just like any production enterprise, the rapid growth in food production has resulted in the substantial increase in wastes and by-products generation along with the entire aquaculture "farm-to-fork" value chain. Only 30–50% of the aqua-farming production are used for direct human consumption. By-products such as fins, scales, skins, and viscera are discarded in a quantity that

Abbreviations: AFM, atomic force microscopy; ALP, alkaline phosphatase; ATR-FTIR, attenuated total reflectance Fourier transform infrared; BDDE, 1,4-butanediol diglycidyl ether; BFCol, American bullfrog skin-derived tropocollagen; BSA, Bovine serum albumin; C_t, threshold cycle; DLS, dynamic light scattering; DMEM/F-12, Dulbecco's Modified Eagle's Medium/Nutrient Mixture F-12 Ham; EDX, energy dispersive X-ray; FBS, fetal bovine serum; FESEM, field emission scanning electron microscope; HA, hydroxyapatite; hFOB 1.19, human fetal osteoblastic 1.19 cell line; IL-6, interleukin 6; IL-23, interleukin 23; LPS, lipopolysaccharides; NaOH, sodium hydroxide; OC, osteocalcin; PBS, phosphate buffered saline; PDF®, Powder Diffraction File™; PMA, phorbol 12-myristate 13-acetate; RPMI-1640, Roswell Park Memorial Institute (RPMI)-1640; RT-PCR, real-time polymerase chain reaction; SDS-PAGE, sodium dodecyl sulphate-polyacrylamide gel electrophoresis; TNF-α, tumor necrosis factor α; XRD, X-ray powder diffraction.

* Corresponding author at: School of Materials Science and Engineering, Nanyang Technological University Singapore, N4.1, 50 Nanyang Avenue, Singapore 639798, Singapore.
E-mail address: cytay@ntu.edu.sg (C.Y. Tay).

https://doi.org/10.1016/j.msec.2021.112104
Received 10 December 2020; Received in revised form 23 March 2021; Accepted 8 April 2021
Available online 17 April 2021

exceeds 20 million tons per year, with the majority either disposed by landfill or incineration [9]. For aquaculture side-streams that do get recycled, they are conventionally reprocessed into fish feed and fertilizers of low economic value. However, the vast amount of aquaculture by-products actually contains numerous valuable bioactive compounds such as peptides, collagen, lipids, and calcium phosphates, which could potentially be exploited for high-value biomedical applications [10]. Therefore, efforts to reduce and valorize waste generated from aquaculture-related activities for the production of high-quality biomaterials have gained significant traction in recent years [11].

Against the backdrop of global climate change and the call for greater sustainability, the "waste-to-resource" paradigm has emerged as an attractive approach to augment efforts in waste management [5]. One of the well-known research directions is the transformation of fish wastes such as fish skins and scales into collagen for soft tissue engineering, including skin and lymphatic vessel regeneration [4,12]. Similarly, natural hydroxyapatite (HA) has been harvested from biowastes such as eggshells, fish scales, and mussel shells targeted for bone tissue engineering [13,14]. In general, an ideal scaffold material for bone tissue engineering should be (i) intrinsically non-toxic to ensure good biocompatibility, (ii) compatible with processing techniques that would enable emulation of the biophysical and biochemical complexity of the host tissue, (iii) porous to optimize cell infiltration and exchange of nutrients/metabolic wastes, (iv) adequate mechanical strength under physiological loading conditions, (v) mechanically and structurally stable to withstand loading and (vi) osteoconductive or osteoinductive to support "*restitutio ad integrum*" recovery [15–17].

Native bone is composed of two pre-dominant components, namely type I collagen (organic phase) and HA (inorganic phase). The collagen provides tensile strength and flexibility to the bone, while HA provides stiffness and hardness [18]. The degree of bone mineralization is site-specific and can vary between 50 and 70% [19]. Recent studies have shown that collagen (extracted from fish skin and scale) enriched with synthetic HA exhibits remarkable bioactive and osteogenic activity [20]. Similarly, a 3D polymethyl methacrylate (PMMA) scaffold reinforced with natural HA (isolated from fish scale) enhances the formation of bone-like apatite [21]. Both collagen and HA have been shown to promote osteoblasts interaction and differentiation, but when combined together, both components act synergistically to enhance osteogenesis [20]. In addition, a porous scaffold is highly needed in guiding cell attachment and growth [22]. As such, 3D porous collagen-HA composites have been developed as a synthetic bone graft targeted for bone tissue regeneration. Apart from the similar structural, compositional, and osteoconductivity properties to that of the bone, composites made of collagen and HA are also expected to be superior from the biomechanical perspective - the ductile properties of the collagenous matrix can better improve fracture toughness and the HA fractions can increase resistance to the 3D swelling, thereby delivering better overall mechanical "wet" properties. The conversion of aquafarming wastes into bone engineering tissue products is highly desirable as it does not only serve as an effective waste management strategy to reduce the environmental impact, but it is also economically feasible to reduce the cost of collagen and HA production.

In this study, we describe the fabrication of a novel hybrid biocomposite derived entirely from aquaculture side-streams. Type I tropocollagen from the skin of American bullfrog (*Rana catesbeiana*; BFCol) and single-phase HA derived from the discarded scales of snakehead fish (*Channa micropeltes*; HA) were exploited to reconstitute the organic and inorganic phases of the bone tissue, respectively. As one of the largest frog species in the world, *Rana catesbeiana* is farmed primarily for its meat, serving as an alternative source of protein. In Singapore alone, the annual consumption of frog flesh was estimated to be around 5 million kilograms, which is equivalent to 15 million frogs per year [23]. Similarly, the annual consumption of fish was estimated to be around 100 million kilograms per year [24]. As such, large amounts of food waste are being generated annually, which could be explored as a sustainable "waste-to-resource" scaffolding biotemplate. The structural stability of the biocomposite consists of BFCol and HA was chemically enhanced using the 1,4-butanediol diglycidyl ether (BDDE) crosslinker (i.e., B-BFCol/HA). *In vitro* analysis was performed with the human fetal osteoblastic 1.19 cell line (i.e., hFOB 1.19) to examine the osteoconductive (osteoblast adhesion and proliferation) and osteogenic differentiation properties of the scaffold.

2. Materials and methods

2.1. Materials

Discarded American bullfrog skins and snakehead scales were kindly provided by KhaiSeng Trading & Fish Farm Pte Ltd. Sodium hydroxide (NaOH), acetic acid, sodium chloride, 1,4-Butanediol diglycidyl ether (BDDE), Dulbecco's Modified Eagle's Medium/Nutrient Mixture F-12 Ham (DMEM/F-12) medium, Roswell Park Memorial Institute (RPMI)-1640 medium, sodium bicarbonate, L-glutamine, phorbol 12-myristate 13-acetate (PMA), lipopolysaccharides (LPS), paraformaldehyde, KAPA SYBR FAST (KK4618), bovine serum albumin (BSA) and Alizarin red S were purchased from Sigma-Aldrich, USA. 10 K MWCO SnakeSkin™ dialysis tubing, antibiotic-antimycotic, Penicillin-Streptomycin, Trypsin-EDTA, Phosphate buffered saline (PBS), Bicinchoninic Acid (BCA) protein assay kit, PrestoBlue™ cell viability reagent, PureLink RNA Mini Kit (12183018A), Alexa Fluor 488 goat anti-rabbit IgG (A11034) and Hoechst 33342 nucleic acid stain were obtained from Thermo Fisher Scientific, USA. 5 mm zirconia balls and 20 μm sieve were obtained from Retsch, Germany. 10% polyacrylamide gel, Bio-Safe™ Coomassie Brilliant Blue R-250, Superscript® III First-Strand Synthesis Supermix, and Triton X-100 were purchased from Bio-Rad, USA. THP-1 monocytes and hFOB 1.19 cells were purchased from ATCC, USA. Fetal bovine serum (FBS) was obtained from Research Instruments Pte Ltd., USA. Ethanol was purchased from Merck Millipore, USA. Rabbit anti-osteocalcin (OC) antibody (ab93876) was obtained from abcam®, USA.

2.2. Collagen recovery from the skins of Rana catesbeiana

Collagen was extracted from *Rana catesbeiana* skins using our in-house developed mechano-chemical method. Briefly, freshly obtained *Rana catesbeiana* skins were first washed with ice-cold water to remove all the impurities. Subsequently, the skins were treated with 0.5 M NaOH at a weight-to-volume ratio of 1:10 over 48 h with a change in NaOH solution every 24 h to remove the non-collagenous proteins. The NaOH-treated *Rana catesbeiana* skins were then thoroughly washed with distilled water and neutralized with HCl to remove the residual NaOH. Thereafter, the skins were soaked in 0.5 M acetic acid at a weight-to-volume ratio of 1:10 overnight to digest the skins, followed by blending using a Philips blender (HR3658/01) at 35,000 rpm for 5 min to produce a thick collagenous paste. The paste was then diluted (1:5) with distilled water, followed by centrifugation at 25,000 $\times g$ for 15 min to separate the pigments from the collagen solution. Collagen was then salted out using 0.9 M of NaCl, in which the collagenous pellet can be collected via centrifugation at 5500 $\times g$ for 15 min. The collagen was then reconstituted in 0.5 M acetic acid and dialyzed against 0.1 M acetic acid using SnakeSkin™ dialysis tubing (10 K MWCO) for 48 h, followed by another round of dialysis in distilled water for 48 h with a change in solution every 24 h. The final solution was subsequently lyophilized and stored at 4 °C until further usage. The entire extraction process was carried out at 4 °C.

2.3. Hydroxyapatite from the scales of Channa micropeltes

HA was harvested and processed from the discarded scales of *Channa micropeltes* via the calcination method, as described previously [14]. Briefly, the scales were calcined in a N7/H muffle furnace (Nabertherm GmbH, Germany) at 850 °C for 1 h with a constant heating rate of 10 °C/

min to remove the organic matter. Following which, the samples were subsequently mixed with 1× PBS at a solid-to-solution ratio of 1:10, followed by ball-milling using 5 mm zirconia balls at a 10% weight-to-weight ratio of HA to zirconia balls for 24 h and air-dried for another 24 h. Thereafter, the ground-up HA was sieved (20 μm pore size) and stored in a dry cabinet for further use.

2.4. One-pot synthesis of B-BFCol/HA hybrid biocomposite

A one-pot synthesis scheme was employed to prepare the B-BFCol/HA hybrid biocomposite. Briefly, the lyophilized collagen (10 mg/mL) was dissolved in 0.5 M acetic acid followed by the addition of the micronized HA powder at a 1:1 collagen-to-HA weight ratio together with 10% w/w BDDE crosslinker (based on the dry weight of collagen), mixed by stirring at 300 rpm for 24 h at 4 °C. To minimize dissolution of HA in the reaction mix, approximately 20 mM of HA was used, which is significantly higher than the reported solubility limit of HA in acetic acid [25]. Thereafter, the reaction mix was either air-dried onto the piranha solution-cleaned coverslips to produce 2D coats or transferred into a mold and lyophilized to produce the 3D porous B-BFCol/HA samples.

2.5. Field emission scanning electron microscopy

Samples were sputtered with a thin layer of platinum (Pt) at 20 mV for 15 s using a JEOL Auto Fine Coater (JFC-1600; JEOL Co., Japan). Following which, the cross-sectional images of the samples were obtained from the JSM-7600F Schottky FESEM (JEOL Co., Japan) at an acceleration voltage of 5 kV at a magnification of ×200, ×15,000, and ×100,000. Pt was selected as the coating materials since it was previously demonstrated that its usage will not interfere with collagen and/or hydroxyapatite analysis [26]. The pore size dimensions were measured using the ImageJ freeware (https://imagej.nih.gov/ij/).

2.6. Attenuated total reflectance Fourier transform infrared (ATR-FTIR) spectroscopy

The samples were placed directly onto the ATR sampling accessory and scanned in a range of 4000–650 cm^{-1} at a resolution of 4 cm^{-1} using a Frontier MIR/FIR spectrometer (Perkin Elmer Inc., USA). The infrared spectrum was captured over 32 scans, where the peaks were used to identify the chemical functional groups. Further analysis was carried out on the obtained spectra to examine the structure of the extracted collagen by measuring the peak intensity ratio between Amide III and 1450 cm^{-1} [4,27].

2.7. Sodium dodecyl sulphate-polyacrylamide gel electrophoresis (SDS-PAGE)

The lyophilized collagen was dissolved in 0.01 M acetic acid at 10 mg/mL followed by mixing with an equal volume of 1× SDS Loading Dye and heated at 95 °C for 5 min to denature the protein. Subsequently, 10 μL of the solution was loaded onto the 10% polyacrylamide gel, where the proteins were separated under a current of 0.2 A for 2 h. Thereafter, the polyacrylamide gel was stained with Bio-Safe™ Coomassie Brilliant Blue R-250 for 1 h before washing with de-staining solution for another 1 h. Finally, a photograph of Coomassie Brilliant Blue-stained polyacrylamide gel was captured to visualize the various protein bands.

2.8. Atomic force microscopy

The topography of the collagen was examined by atomic force microscopy (AFM). The collagen solution (1 μg/mL) was air-dried on a mica surface before scanning at 500 mV using a Cypher S atomic force microscope (Asylum Research, USA) under tapping mode with a scan rate of 1.0 Hz and scan size of 1.30 × 1.30 μm^2 square area.

2.9. Energy dispersive X-ray (EDX) spectroscopy

The samples were sputter-coated with a thin layer of Pt using Fine Coater JFC-1200 (JEOL Co., Japan), where the elemental spectrum was collected by area mapping at a magnification of ×100 under 10 kV using the JSM-7600F Schottky field emission scanning electron microscope (FESEM; JEOL Co., Japan). The calcium-to-phosphate ratio was then calculated based on the compositional analysis obtained from the elemental spectrum.

2.10. X-ray powder diffraction (XRD) analysis

The XRD profile of HA was obtained by scanning the sample under theta/2theta mode using Shimadzu XRD-6000 (Shimadzu Corp., Japan) in a range of $20 < 2\theta < 60$ with a scan speed of 1°/min and a step size of 0.05°. The XRD profile was then compared to the powder diffraction database (International Centre of Diffraction Data) to determine the chemical phases present in the HA.

2.11. Dynamic light scattering (DLS) particle size measurement

The particle size distribution of the HA was analyzed using a high-performance particle nanosizer (Malvern Zetasizer – Nano ZS; Malvern Instruments, UK). 1 mg of the obtained powders was mixed with 100 mL of distilled water followed by sonication. Subsequently, 1 mL of the solution was transferred into a plastic disposable cuvette and placed inside the sample holder for particle size measurements.

2.12. Porosity measurement

The porosity of the 3D hybrid biocomposites was measured using a liquid displacement method. Briefly, the individual sample was immersed in a glass bottle containing a known volume of absolute ethanol (V1) for 5 min. Subsequently, the total volume of absolute ethanol with the ethanol-impregnated sample was recorded as V2. The ethanol-impregnated sample was then removed from the glass bottle, where the residual ethanol volume was recorded as V3. The porosity of the scaffold was then estimated according to Eq. (1).

$$Porosity = \frac{V1 - V3}{V2 - V3} \times 100\% \quad (1)$$

2.13. Compression modulus

The mechanical property of the 3D hybrid biocomposites was determined by measuring the compression modulus of the samples. The cylindrical-shaped samples with standard width: 8.95 mm and length: 17.90 mm were loaded onto an Instron universal testing machine (Model 5567; Instron Corp., USA) and compressed to 50% of its original height at a rate of 2 mm/min using a 10 kN load cell to obtain a stress-strain curve. The initial gradient of the stress-strain curve was then measured as the compression modulus.

2.14. Microindentation Vickers hardness

A Vickers hardness test was carried out on the 3D hybrid biocomposites using ZwickRoell Indentec ZHVμ Micro Vickers with 0.2 kgf load for 10 s, in which the Vickers hardness was estimated according to Eq. (2).

$$HV = \frac{2F\ sin\frac{136°}{2}}{d^2} \quad (2)$$

where F is the load in kgf and d is the arithmetic mean of the two diagonals (d1 and d2) in mm.

2.15. Cell culture

THP-1 monocytes were cultured and expanded in RPMI-1640 medium supplemented with 10% FBS, 1.6 g/L sodium bicarbonate, and 1% Penicillin-Streptomycin under 37 °C, 5% CO_2 environment, and saturated humidity. The immunoreactivity of the hybrid biocomposites was examined using PMA differentiated macrophages from human THP-1 monocytes, where the pro-inflammatory genes expressed by THP-1 macrophages were examined using real-time polymerase chain reaction (RT-PCR) [28]. hFOB 1.19 cells were cultured and expanded using DMEM/F-12 medium supplemented with 10% FBS, 1× antibiotic-antimycotic, 1.6 g/L sodium bicarbonate, and 2.5 mM L-glutamine under 34 °C, 5% CO_2 environment, and saturated humidity to evaluate the bioactive and osteogenic properties of the hybrid biocomposites. For cell culture studies, the samples were sterilized by ethylene oxide (EtO) gas treatment using an EOGas 4 sterilizer (Andersen Products, Inc., USA) overnight.

Total RNA was extracted from cells using the PureLink RNA Mini Kit. The concentration and quality of the total RNA were determined using NanoDrop™ 2000 (Thermo Scientific, USA). Thereafter, synthesis of cDNA was carried out on the extracted RNA using iScript cDNA Synthesis Kit according to manufacturer's protocol, where the reaction was done using a T100 Thermal Cycler (Bio-Rad, USA): Priming for 5 min at 25 °C, reverse transcription for 20 min at 46 °C, and reverse transcriptase inactivation for 1 min at 95 °C. For the RT-PCR experiment, KAPA SYBR FAST was used where the expression levels of the target mRNA transcripts were determined using a CFX Connect RT-PCR Detection System (Bio-Rad, USA) using the following protocol: enzyme activation and DNA denaturation at 95 °C for 30 s, followed by amplification for 40 cycles, with each cycle including 15 s of denaturation step at 95 °C, as well as 30 s of annealing/extension and plate reading at 60 °C. The threshold cycle (C_t) values were noted for each transcript and normalized to the internal housekeeping control. The relative quantitation of each mRNA was performed using the comparative C_t method as described earlier [29]. The listed sequence of the primers (Table 1) was obtained from primer bank (https://pga.mgh.harvard.edu/primerbank). For the immunogenic response study, 1 μg/mL LPS was used as a positive control to induce polarization of resting macrophages (M0) to proinflammatory M1 phenotype. Meanwhile, the osteo-related ALPL and BGLAP expressions of hFOB 1.19 cells were determined using the same protocol by harvesting the RNA from the hFOB 1.19 cells seeded on different 2D hybrid biocomposite samples on different pre-determined time points.

2.16. Cell proliferation assay

The proliferation of hFOB 1.19 cells was determined using the PrestoBlue™ cell viability reagent at various pre-determined time points according to the manufacturer's recommended protocol. Briefly, the cells were seeded onto the 2D (i.e., collagen-coated 24-well plate surface) and 3D (i.e., cylindrical-shaped sample with standard width: 3.2 mm and length: 6.3 mm) samples with a seeding density of 30 k cells/cm^2 and 600 k cells/mL, respectively. At pre-determined time points, the number of cells was measured by incubating the cell-seeded samples with 10% v/v PrestoBlue™ reagent for 1 h at 37 °C. At the end of the incubation period, 200 μL of the solution was transferred into a 96-well plate where the fluorescence intensity (Ex 560/Em 590 nm) was measured using a SpectraMax M2 microplate reader (Molecular Devices, USA). Cell number was determined using a standard curve correlating the fluorescence intensity to the known number of cells. Further analysis was carried out to compare the population doubling rate of the hFOB 1.19 cells cultured on different samples according to Eq. (3).

$$Cell\ doubling = \frac{ln(Nf) - ln(Ni)}{ln(2)} \tag{3}$$

where N_f is the cell count obtained at the respective time point, and N_i denotes the cell count acquired from the previous time point.

Table 1
Sequences of primers and housekeeping genes used for RT-PCR studies.

Transcripts	Primer sequence (5′ to 3′)
IL-6	GTAGCCGCCCCACACAGA
	CATGTCTCCTTTCTCAGGGCTG
IL-23	TGCAAAGGATCCACCAGGGTCTGA
	TAGGTGCCATCCTTGAGCTGCTGC
TNF-α	ATGAGCACTGAAAGCATGATC
	TCACAGGGCAATGATCCCAAAGTAGACCTGCCC
ALPL	CGTTGTCTGAGTACCAGTCCC
	ACCACCACGAGAGTGAACCA
BGLAP	CACTCCTCGCCCTATTGGC
	CACTCCTCGCCCTATTGGC
18S	GCGGCGGAAAATAGCCTTTG
	ATCACACGTTCCACCTCATCC

2.17. Immunocytochemical staining

The hFOB 1.19 cells seeded on 2D hybrid biocomposite samples were fixed with 4% paraformaldehyde for 12 h at 4 °C on pre-determined time points. Subsequently, the cells were permeabilized with 0.2% Triton X-100 for 10 min at room temperature. The samples were then washed with 1× PBS three times before the samples were blocked with 2% BSA solution for 1 h at room temperature. Rabbit anti-OC antibody at a dilution factor of 1:500 was added to the samples and incubated for 12 h at 4 °C. Following this, the samples were washed with 1× PBS three times and incubated with Alexa Fluor 488 goat anti-rabbit IgG (H + L) at a dilution factor of 1:500 with 0.2 μg/mL of Hoechst 33342 solution for 2 h at room temperature in the dark. The immuno-stained images were viewed and imaged via the Zeiss Axio Imager Z1 (Carl Zeiss, Germany) inverted epifluorescence microscope fitted with an Axiocam HRM camera. To facilitate cross-comparison of the samples, imaging conditions such as exposure duration, signal amplification, etc., were kept constant. Expression levels of the target proteins were processed and measured with the ImageJ freeware (https://imagej.nih.gov/ij/).

2.18. Alizarin red S staining

The cell-seeded 3D hybrid biocomposite samples were cryosectioned and stained with Alizarin red S. Briefly, the cell-seeded samples were fixed using 4% paraformaldehyde for 12 h at 4 °C. Subsequently, the fixed samples were washed three times with 1× PBS, followed by immersing in FSC 22 Frozen Section Media and frozen at −20 °C. The samples were then cryosectioned into 10 μm sections using microtome, where the samples were collected and adhered onto poly-L-lysine treated glass slides. The samples were then washed three times with 1× PBS, followed by incubating with 40 mM of Alizarin red S solution prepared using distilled water with a final pH of 4.1 for 24 h. At the end of the process, the samples were washed thoroughly with distilled water until the wash water was nearly clear. Finally, the cleaned samples were imaged using a light microscope to visualize the calcium in the sections.

2.19. Statistical analysis

All experiments were carried out in triplicate (n = 3) and expressed as mean ± standard deviation unless otherwise specified. The statistical significance was analyzed using Kruskal-Wallis non-parametric one-way analysis of variance and Mann-Whitney *U* test, where the data was considered statistically significant with $p < 0.05$.

3. Results and discussion

3.1. Extraction and characterization of American bullfrog skin collagen

In general, animal and marine based collagen can be extracted via chemical (e.g., acid, alkaline, etc.) and enzymatic (e.g., pepsin) hydrolysis [30]. Both approaches are amendable for mass-production as the collagen-rich homogenized tissues are systematically broken down to isolate the solubilized collagen fibers. The extractability of the collagen with physical treatment by means of mechanical homogenization and ultrasonication to increase surface for mass transfer has been explored [31]. Specific to this study, an optimized combinatorial mechano-chemical collagen extraction protocol (Fig. 1A) was employed. The bullfrog skin was first ground and homogenized prior to acid treatment. As shown in Fig. 1B, the final lyophilized BFCol takes on a whitish appearance, suggesting the successful removal of the skin pigments. Using this approach, we were able to obtain 70.0 ± 7.5% w/w collagen yield, which to our knowledge is by far the highest reported yield from frog skin [30,32,33]. Furthermore, in-house benchmarking against the traditional acetic acid solubilization method revealed that the developed strategy not only improves the extraction yield by approximately 300%, but could also significantly shorten the extraction time from 19 days to 11 days (data not shown). The reduction in the extraction solvent usage could therefore potentially decrease the amount of wastewater generated, thereby reducing the overall environmental footprint of the process (data not shown). ATR-FTIR spectrum of BFCol showed absorption peaks that are characteristics of amide A (~3300 cm^{-1}), amide B (~2920 cm^{-1}), amide I (~1630 cm^{-1}), amide II (~1530 cm^{-1}), and amide III (~1200 cm^{-1}) (Fig. 1C) [4]. Additionally, the absorbance peak intensity ratio of amide III band to 1450 cm^{-1} was found to be around 1, which is indicative of the triple helix conformation in BFCol [4]. SDS-PAGE analysis revealed several distinct bands near 250, 139, and 129 kDa (Fig. 1D), corresponding to the β-, α1- and α2-chains, respectively. In addition, the ratio of the α1- and α2-chains was found to be 2-to-1, similar to that of type I collagen [27]. Notably, the acid soluble fraction of the BFCol exists as nanofibers with a diameter of approximately 20–25 nm and a length of 200–400 nm, which could correspond to small aggregates of tropocollagen (Fig. 1E) [34]. Compared to the typical micron-sized collagen fibrils, the presentation of nano-scale BFCol could enhance cell-material interactions and better support fundamental cellular processes such as proliferation, migration, and differentiation, which are advantageous for tissue engineering applications [35,36].

3.2. Preparation and characterization of snakehead scale-derived HA

Calcium phosphate minerals, mainly in the form of HA, are the main inorganic component of bones that are required to osteoconduct and regulate activation of osteoblasts for bone regeneration [37]. Specific to this study, HA was prepared from the scales of *Channa micropeltes* by heating at 850 °C to remove the organic compounds and to prevent HA to β-tricalcium phosphate transformation (Fig. 2A) [14]. The extraction yield of the resultant calcined product is 41.9 ± 5.3% w/w, which is

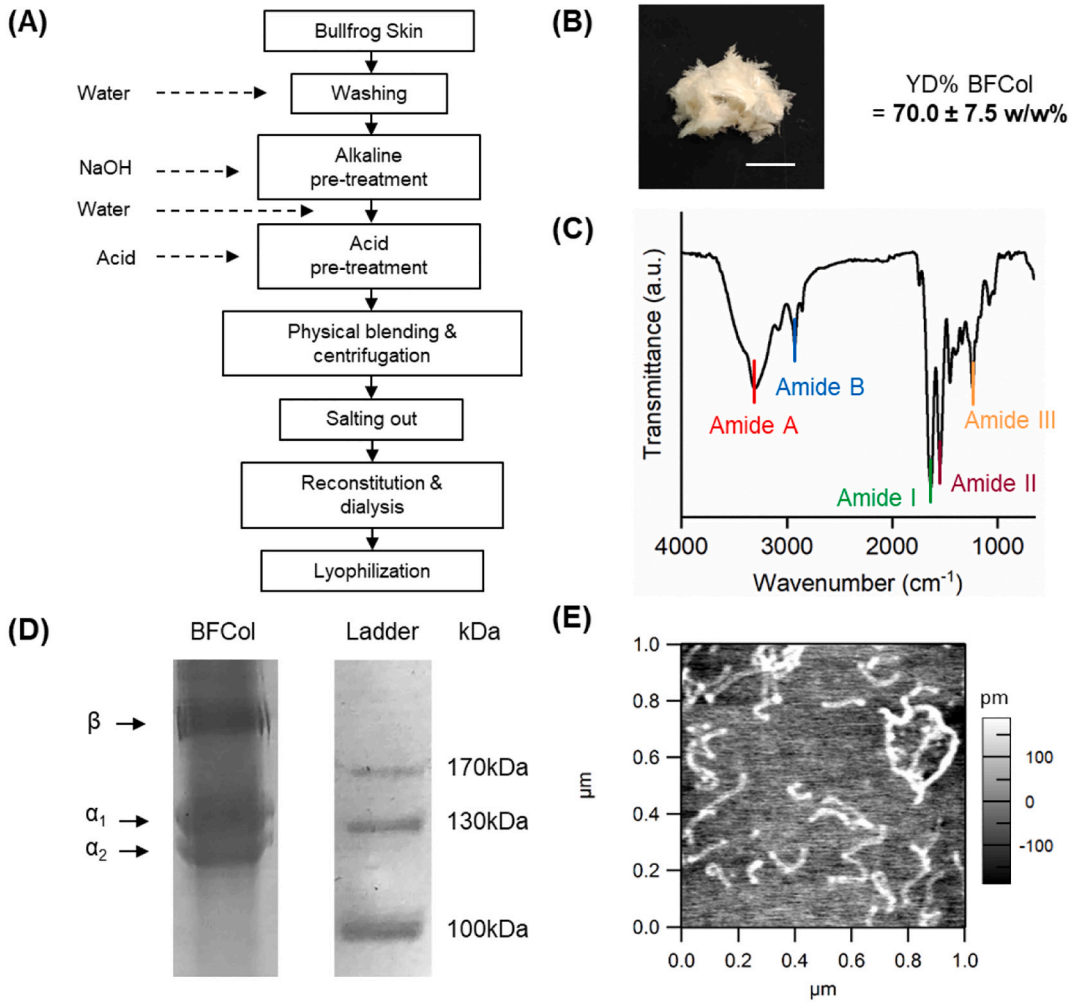

Fig. 1. Extraction and characterization of BFCol. A) Schematic depicting extraction process employed to recover collagen from bullfrog skins. B) Optical photograph of the lyophilized collagen. Scale bar = 1 cm. C) ATR-FTIR spectrum, D) SDS-PAGE, and E) AFM analysis of the extracted BFCol nanofibrils.

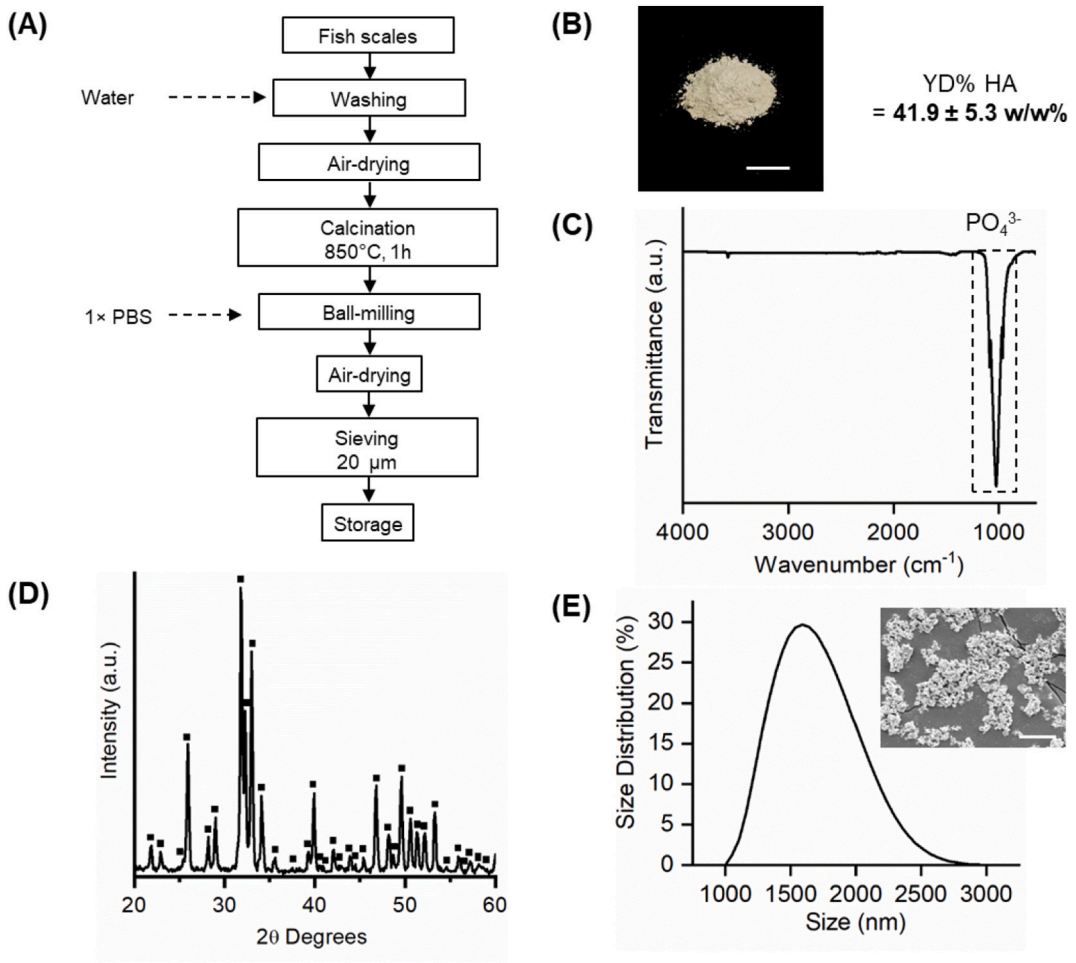

Fig. 2. Extraction and characterization of fish scale-derived HA. A) Schematic depicting the processes involved in the isolation of HA from fish scales. B) Optical photograph of the HA. Scale bar = 1 cm. C) ATR-FTIR spectrum of the HA. D) XRD profile of the monophase HA. E) DLS analysis showing the average particle size of the isolated HA. Scale bar = 5 μm.

close to the reported total inorganic components found in fish scales (40–45 wt%) [38]. Based on EDX analysis, the calcium-to-phosphate ratio of the extracted FSHA was determined to be approximately 1.66, which is close to the stoichiometric ratio for HA of 1.67 (Fig. 2B) [14]. ATR-FTIR spectrum (Fig. 2C) showed characteristic phosphate absorption peaks in the region of 1100 to 960 cm^{-1} while the occurrence of organic peaks are visibly absent, suggesting that the sample is devoid of organic residues. Furthermore, the XRD pattern of the snakehead scale derived HA matched well with the single-phase HA from the Powder Diffraction File™ (PDF®) database (Fig. 2D). Finally, DLS analysis revealed that the HA sample has an average hydrodynamic diameter of ~1.6 μm (Fig. 2E), which falls within the reported optimum size range (i.e., 1–10 μm) that favors bone cell interactions and bone tissue integrations [39].

3.3. Physicochemical characterization of B-BFCol/HA hybrid biocomposite

Despite their excellent biocompatibility, the application of marine collagen has been limited in tissue engineering due to its low denaturation temperature (≤30 °C) and poor physicochemical properties [40]. Comparatively, the documented denaturation temperature of BFCol is higher at ~43 °C, which is a unique characteristic that is advantageous for biomedical applications [27]. To further improve the mechanical properties, the BFCol network is structurally stabilized using the biocompatible epoxide-based bifunctional crosslinker, BDDE (10 w/w% based on the dry weight of collagen). Mechanistically, the two epoxy terminals of BDDE can react with the free carboxyl groups present in the collagen molecules to form ether bonds, while the BDDE backbone serves as the linkage between adjacent collagen chains. Successful crosslinking of the samples was first confirmed by ATR-FTIR, with the additional ether peak (C-O-C) being observed within the range of 1050 and 1250 cm^{-1} after the crosslinking process (Fig. 3A). The presence of HA in the B-BFCol/HA hybrid biocomposite was detected by the increase in the peak intensity between 1040 and 1100 cm^{-1}, that is associated with the phosphate (PO_4^{3-}) functional group. This was further confirmed by the FESEM images shown in Fig. 3B. While both the B-BFCol and B-BFCol/HA samples displayed highly interconnected and porous architecture, the occurrence of micronized HA was limited to the B-BFCol/HA group. The average pore size of B-BFCol/HA hybrid biocomposites was found to be ~54.6 ± 26.3 μm, within the suitable pore size range (i.e., 20–1500 μm) for tissue engineering applications [41]. At higher magnifications, the presence of HA micro-agglomerates against the chemically crosslinked BFCol nanofibrous network was clearly evident. The presence of these HA micro-agglomerates not only modulates the surface chemistry in promoting osteoblast proliferation and differentiation [42], but the increased surface roughness may also enhance cell adhesion and spreading [43]. For instance, a recent study by Zheng *et al.* had shown that the presentation of micro-nano topographies on Ti-6Al-4V surface could promote osteoblasts adhesion and differentiation via the integrin-associated α2-PI3K-AKT signaling axis [44]. Additionally, the "designed-in" surface roughness was also observed to significantly increased the

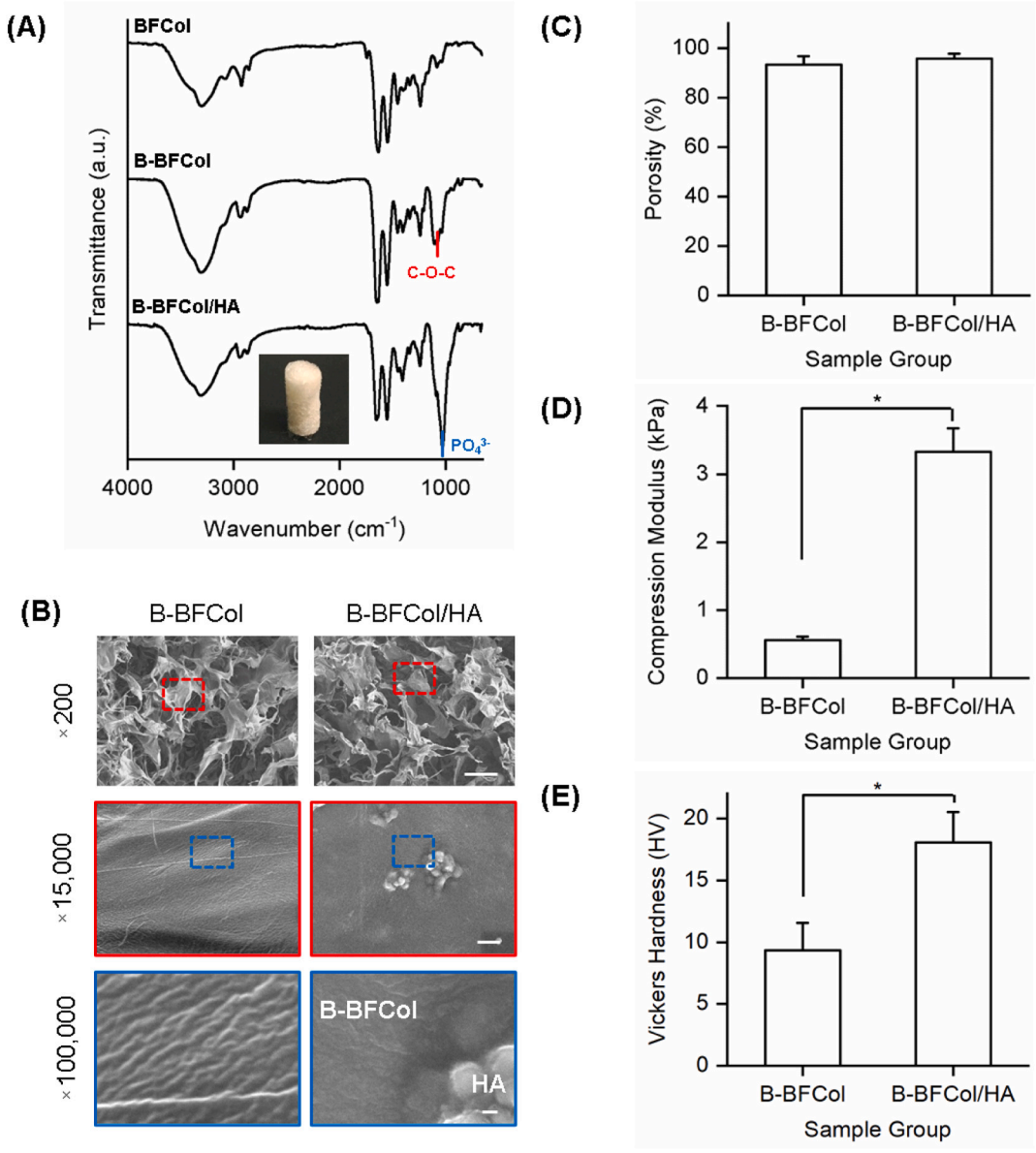

Fig. 3. Characterization of BFCol/HA hybrid biocomposite. A) ATR-FTIR spectra, B) cross-sectional SEM images, C) porosity measurements, D) comprehensive modulus measurements, and E) Vickers hardness measurements of BFCol, B-BFCol and B-BFCol/HA samples. Scale bar = 100 μm (×200), 1 μm (×15,000), and 1 nm (×100,000). All samples were characterized in triplicates. * denotes statistical difference between indicated experimental groups at $p < 0.05$.

hydrophilicity of the B-BFCol/HA (23.4 ± 4.8°) compared to the B-BFCol control (56.8 ± 4.6°), which could further improve protein adsorption and ALP expression of osteoblast cells (Supplementary Fig. S1) [45,46].

In addition, the porosity of both the B-BFCol and B-BFCol/HA samples are in excess of 90% (Fig. 3C). This finding is in agreement with the fully interconnected network and porous architecture as revealed from the FESEM images (Fig. 3B). Highly porous scaffolds are attractive from the tissue engineering standpoint as they facilitate cell penetration, nutrients, and metabolic waste exchange, vascularization, as well as bone formation [47]. Notably, compared to the B-BFCol control group, the compression modulus of the B-BFCol/HA scaffold was approximately 6-fold stiffer (Fig. 3D). The mechanical properties of the scaffold are important to ensure long-term structural and functional viability [48]. The addition of micronized fish scale derived HA coupled with BDDE crosslinking significantly increased the compressive stiffness of B-BFCol/HA hybrid biocomposite. Specifically, the measured bulk compressive stiffness of B-BFCol/HA was estimated to be around 3.32 ± 0.35 kPa. Although the scaffolding modulus for the formation of the osteoblastic matrix is in the range of 30 kPa [49], the presence of bioactive components can induce a greater biochemical effect on the osteogenesis in which a soft substrate is amendable to support stem cell osteogenic differentiation [50]. Nevertheless, the matrix stiffness of the hybrid biocomposite can be enhanced by either incorporating nano-sized HA (~ 6.2-fold increase in compressive modulus) rather than micron-sized HA (~2.2-fold increase in compressive modulus) or coating the porous scaffold with HA precipitate (~26.2-fold increase in compressive modulus) to further fine-tune the physical properties [51]. Consistent with the bulk measurements, microindentation Vickers tester data showed that B-BFCol/HA (18.0Hv/0.2) exhibited an approximately 2-fold higher surface hardness relative to the B-BFCol matrix alone (Fig. 3E). Taken together, the presence of nano-HA could augment the compressive modulus and substrate stiffness which may help to promote interactions with bone cells [52]. Moreover, the B-BFCol/HA hybrid biocomposite displayed excellent absorbency, making it ideal to absorb bodily fluid and maintain a moist microenvironment supportive of tissue

repair (Supplementary Video). Furthermore, we noted that the incorporation of the HA is beneficial to improve the biodegradability of the scaffold, which is critical to cell ingrowth, host response, and bone mineralization and regeneration (Supplementary Fig. S2) [22]. The improved degradation profile of the B-BFCol/HA scaffold could be attributed to the decreased levels of collagen crosslinking, as a result of the increased BFCol-HA interface. Collectively, the high porous structural fidelity, coupled with the improved mechanical properties, makes B-BFCol/HA hybrid biocomposite a promising platform for tissue engineering applications.

3.4. *In vitro evaluation of B-BFCol/HA hybrid biocomposite*

Following implantation of biomaterials, host reaction such as inflammation driven by the activation of immune cells (e.g., monocytes, macrophages, etc.) is common. However, the unresolved inflammatory response could be detrimental and may lead to bone loss and implant-tissue disintegration [53]. Therefore, to ensure that our extraction protocol and one-pot synthesis of B-BFCol/HA are suitable for the preparation of implant purposes, the immunoreactivity of hybrid biocomposite was first examined using PMA-induced differentiated macrophages from human THP-1 monocytes. In contrast to the LPS-positive control, the expression level of inflammatory mRNA transcripts such as IL-6, IL-23, and TNF-α of the B-BFCol/HA hybrid biocomposite exposed macrophage remained relatively modest, suggesting that the risk of waste-derived biomaterial hybrid to trigger an excessive acute inflammatory response is low (Fig. 4A). Next, the biological performance of the B-BFCol/HA scaffold for bone repair was assessed with hFOB 1.19 osteoblast cells as the *in vitro* cell model. As seen from Fig. 4B, hFOB 1.19 seeded in B-BFCol/HA 3D porous scaffold exhibited a positive proliferation profile with an increasing number of cells observed over 7 days of culture, but not on the B-BFCol sample. Interestingly, not only is the rate at which the cells are proliferating significantly faster (specific doubling rate of ~0.18 day^{-1} for B-BFCol/HA vs. −0.05 day^{-1} for B-BFCol), but the total number of cells colonizing the B-BFCol/HA scaffold was clearly higher (~169 k for B-BFCol/HA vs. ~98 k for B-BFCol). The significant increase in cell number could be attributed to an improved cell-material interactions with the HA functionalized scaffold [54] or increased in ECM mechanics that can foster cellular proliferation-promoting signal transduction such as mitogen-activated protein kinase/extracellular-signal-regulated kinase (MAPK/ERK) pathways [55]. Consistently, by the end of the 7 days culture, the coverage of hFOB 1.19 was evidently widespread and uniformly distributed (DAPI-stained nuclei) within the B-BFCol/HA scaffold due to the high water-absorbance capacity of the hybrid biocomposite (Fig. 4C). Compared to concentration-matched BDDE crosslinked bovine collagen (B-BVCoL) functionalized with fish scale HA or synthetic HA (SynHA) (~150 nm), the hFOB 1.19 displayed similar growth characteristics after 7 days of culture (Supplementary Fig. S3). This suggests that the cell adhesion and proliferation supporting function of B-BFCol/HA in on par with conventional collagen and HA sources.

Thus far, our *in vitro* findings have shown that the B-BFCol/HA hybrid biocomposite is non-toxic, non-immunogenic, and capable of supporting osteoblasts adhesion, proliferation, and migration. To evaluate the osteoinductive potential of the B-BFCol/HA, hFOB 1.19 osteoblasts were seeded onto the hybrid biocomposite and expression levels of osteogenic mRNA transcript were determined via RT-PCR. ALPL gene encodes the isoenzyme alkaline phosphatases, an early and transient

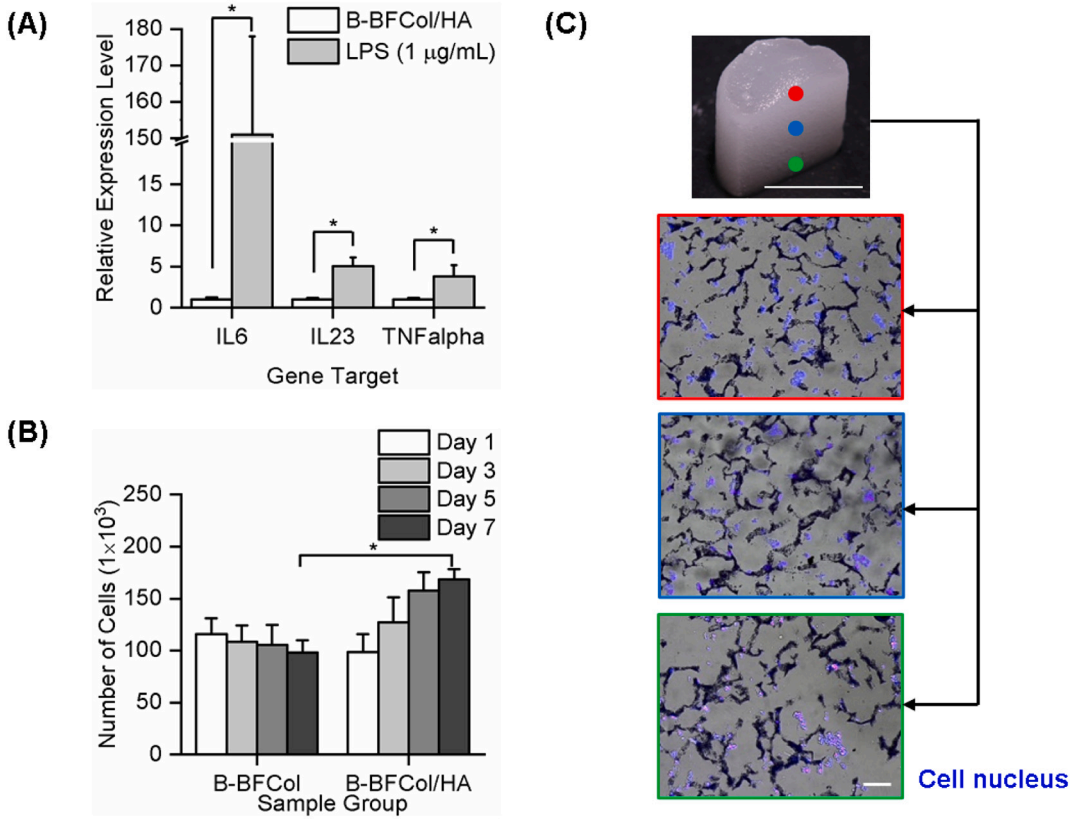

Fig. 4. Cytocompatibility analyses of B-BFCol/HA hybrid biocomposite. A) Expression level of inflammatory mRNA transcripts in macrophage exposed to B-BFCol/HA hybrid biocomposite. B) Quantitative measurement of the hFOB 1.19 growth in B-BFCol/HA hybrid biocomposite over 7 days of culture. C) Cross-sectional microscopic images of the hFOB 1.19-seeded hybrid biocomposite. The cell nucleus (blue) was counter-stained with DAPI dye. Scale bar = 5 mm (optical photograph) and 100 μm (microscopic image). * denotes statistical difference between indicated experimental groups at $p < 0.05$. (For interpretation of the references to colour in this figure legend, the reader is referred to the web version of this article.)

marker of osteogenesis [56]. On the other hand, osteocalcin, which is encoded by the BGLAP gene is an important non-collagenous secreted factor involved in bone matrix mineralization and a late marker for bone formation [57]. In the case of the B-BFCol/HA group, we observed a significant increase in the expression level of ALP (~9.4 fold) relative to the B-BFCol group 14 days into the experiments (Fig. 5A). Thereafter, the upregulated state of ALP was slightly lowered (~2.1 fold) after 21 days of culture. Similarly, BGLAP mRNA transcript (Fig. 5B) and immunocytochemical staining of OC (Fig. 5C) are consistently expressed at a higher level for B-BFCol/HA compared to the B-BFCol group by a factor of 2 to 3-fold on either day 14 or 21. After 21 days of culture period, while the B-BFCol only scaffold showed a modest level of Alizarin red S-positive mineralized deposits, the B-BFCol/HA samples clearly displayed more comprehensive coverage and deeper mineralization staining. Alizarin red S stain quantification showed significantly increased (~1.5 fold) staining for the B-BFCol/HA group compared to the B-BFCol only group (Fig. 5D). This observation is consistent with earlier reports, which showed that HA functionalized type I collagen scaffolds can significantly stimulate the production of mineralized ECM in primary and bone marrow mesenchymal stem cells derived osteoblasts after 7–10 days of culture [58,59]. Comparing the day 7 and day 14 B-BFCol/HA samples, we could observe a slight increase in calcium

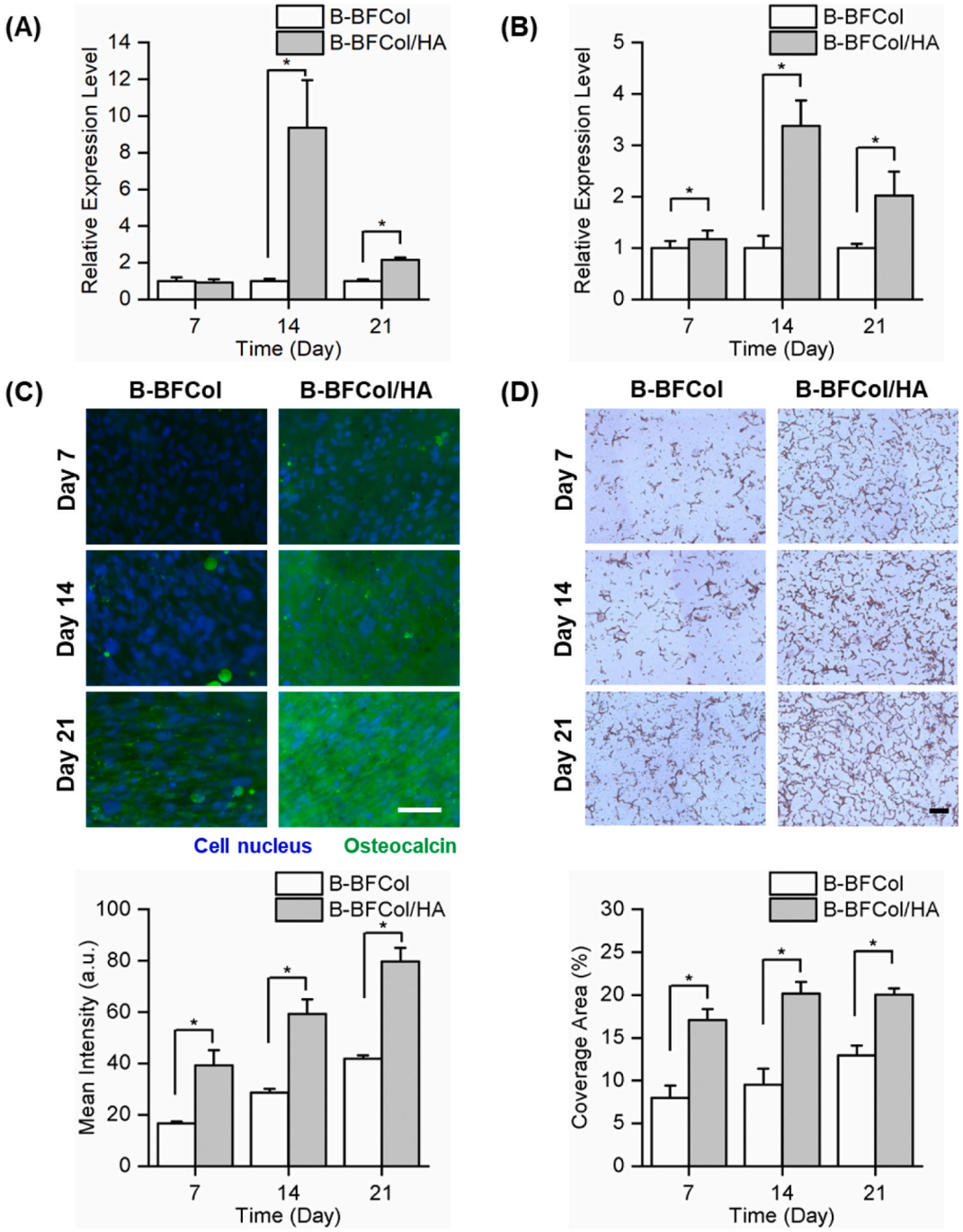

Fig. 5. Osteogenic studies of B-BFCol/HA hybrid biocomposite. A) Expression of early osteoblast marker (ALPL) in hFOB 1.19. B) Expression of late osteoblast marker (BGLAP) in hFOB 1.19. C) Immunocytochemical staining images of hFOB 1.19 counter-stained for cell nucleus (blue) and osteocalcin (green). Scale bar = 100 μm. D) Alizarin red S (red) staining of cell-seeded hybrid biocomposite. Scale bar = 200 μm. * denotes statistical difference between indicated experimental groups at $p < 0.05$. (For interpretation of the references to colour in this figure legend, the reader is referred to the web version of this article.)

deposit (Fig. 5D). However, there is little difference for the Alizarin red S (red) staining between the day 14 and day 21 samples. This is consistent with the pro-osteogenic properties of the scaffold, as calcium deposition by the osteoblasts was previously demonstrated to peak as early as day 14 to form a uniform and stable matrix by Chen *et al.* [60]. Overall, these results are encouraging as they strongly suggest that B-BFCol/HA scaffold is able to support the entire spectrum of bone tissue development – from osteoblasts proliferation, through to extracellular matrix (ECM) synthesis, and on to cell-mediated mineralization.

4. Conclusion

In summary, a sustainable highly porous physio-mimetic tissue engineering scaffold has been developed using a facile and cost-effective one-pot synthesis scheme. The scaffold is comprised entirely of BDDE crosslinked aquafarming side stream wastes, namely, bullfrog skin type 1 tropocollagen nanofibers as the main biotemplate and micronized HA processed from snakehead scale. The B-BFCol/HA scaffold displayed excellent biocompatibility, improved mechanical properties, and enhanced bioactivity due to the presence of osteoinductive HA. An important next step is meaningful *in vivo* implantation studies to establish the long-term tissue responses of the hybrid scaffold and the ability to repair intrabony defects. Nonetheless, these osteo-promoting properties coupled with the *in vitro* proof-of-concept results, have demonstrated the real potential of B-BFCol/HA hybrid biocomposite as a promising "waste-to-resource" bone graft substitute material for bone repair and regeneration.

Supplementary data to this article can be found online at https://doi.org/10.1016/j.msec.2021.112104.

CRediT authorship contribution statement

WANG, J.K.: Conceptualization, Formal analysis, Writing - original draft, Writing - review & editing. Çimenoğlu, Ç and Cheam, N.M.J.: Conceptualization, Formal analysis, Writing - review & editing. Hu, X.: Writing - review & editing. Tay, C.Y.: Conceptualization, Supervision, Formal analysis, Writing - review & editing.

Declaration of competing interest

The authors declare that they have no known competing financial interests or personal relationships that could have appeared to influence the work reported in this paper.

Acknowledgements

The authors gratefully acknowledge support from the Singapore Ministry of Education (MOE) Academic Research Fund Tier 1 (RG38/20 2020-T1-001-152). The American bullfrog skins and snakehead scales were kindly provided by KhaiSeng Trading & Fish Farm Pte. Ltd., Singapore. The authors would also like to acknowledge the Facility for Analysis, Characterization, Testing and Simulation (FACTS), Nanyang Technological University, Singapore, for the use of their electron microscopy facilities.

References

[1] C. Wan, G.Q. Shen, S. Choi, Waste management strategies for sustainable development, in: W. Leal Filho (Ed.), Encyclopedia of Sustainability in Higher Education, Springer International Publishing, Cham, 2019, pp. 1–9.
[2] P. Shi, Y. Wan, A. Grandjean, J.-M. Lee, C.Y. Tay, Clarifying the in-situ cytotoxic potential of electronic waste plastics, Chemosphere 269 (2020), 128719.
[3] X. Tian, B. Zhang, J. Hou, M. Gu, Y. Chen, In situ preparation and unique electrical behaviors of gold@ hollow polyaniline nanospheres through recovery of gold from simulated e-waste, Bull. Chem. Soc. Jpn. 93 (3) (2020) 373–378.
[4] J.K. Wang, K.P. Yeo, Y.Y. Chun, T.T.Y. Tan, N.S. Tan, V. Angeli, C. Choong, Fish scale-derived collagen patch promotes growth of blood and lymphatic vessels in vivo, Acta Biomater. 63 (2017) 246–260.
[5] Z. Wu, T. Soh, J.J. Chan, S. Meng, D. Meyer, M. Srinivasan, C.Y. Tay, Repurposing of fruit peel waste as a green reductant for recycling of spent lithium-ion batteries, Environ. Sci. Technol. 54 (15) (2020) 9681–9692.
[6] R. Meys, F. Frick, S. Westhues, A. Sternberg, J. Klankermayer, A. Bardow, Towards a circular economy for plastic packaging wastes–the environmental potential of chemical recycling, Resour. Conserv. Recycl. 162 (2020), 105010.
[7] S. Luhar, T.-W. Cheng, I. Luhar, Incorporation of natural waste from agricultural and aquacultural farming as supplementary materials with green concrete: a review, Compos. Part B 175 (2019), 107076.
[8] F.a.A.O.o.t.u. Nations, The state of the world fisheries and aquaculture. http://www.fao.org/state-of-fisheries-aquaculture, 2018. (Accessed 17 April 2020).
[9] G. Caruso, Fishery wastes and by-products: a resource to be valorised, J. Fish. Sci. 9 (4) (2015) 80–83.
[10] P. Ideia, J. Pinto, R. Ferreira, L. Figueiredo, V. Spínola, P.C. Castilho, Fish processing industry residues: a review of valuable products extraction and characterization methods, Waste Biomass Valorization (2019) 1–24.
[11] C. Xu, M. Nasrollahzadeh, M. Selva, Z. Issaabadi, R. Luque, Waste-to-wealth: biowaste valorization into valuable bio (nano) materials, Chem. Soc. Rev. 48 (18) (2019) 4791–4822.
[12] A. Afifah, O. Suparno, L. Haditjaroko, K. Tarman, Utilisation of fish skin waste as a collagen wound dressing on burn injuries: a mini review, in: IOP Conference Series: Earth and Environmental Science, IOP Publishing, 2019, p. 012031.
[13] S.-L. Bee, Z.A.A. Hamid, Hydroxyapatite Derived From Food Industry Bio-wastes: Syntheses, Properties and Its Potential Multifunctional Applications, Ceramics International, 2020.
[14] Y.Y. Chun, J.K. Wang, N.S. Tan, P.P.Y. Chan, T.T.Y. Tan, C. Choong, A Periosteum-inspired 3D hydrogel-bioceramic composite for enhanced bone regeneration, Macromol. Biosci. 16 (2) (2016) 276–287.
[15] T. Ghassemi, A. Shahroodi, M.H. Ebrahimzadeh, A. Mousavian, J. Movaffagh, A. Moradi, Current concepts in scaffolding for bone tissue engineering, Arch. Bone Joint Surg. 6 (2) (2018) 90.
[16] K. Glenske, P. Donkiewicz, A. Köwitsch, N. Milosevic-Oljaca, P. Rider, S. Rofall, J. Franke, O. Jung, R. Smeets, R. Schnettler, Applications of metals for bone regeneration, Int. J. Mol. Sci. 19 (3) (2018) 826.
[17] X. Zhang, J. Zhou, H. Ying, Y. Zhou, J. Lai, J. Chen, Glycogen as a cross-linking agent of collagen and nanohydroxyapatite to form hydrogels for bMSC differentiation, ACS Sustain. Chem. Eng. 8 (4) (2020) 2106–2114.
[18] S. Siswanto, D. Hikmawati, U. Kulsum, D.I. Rudyardjo, R. Apsari, A. Aminatun, Biocompatibility and osteoconductivity of scaffold porous composite collagen–hydroxyapatite based coral for bone regeneration, Open Chem. 18 (1) (2020) 584–590.
[19] B. Clarke, Normal bone anatomy and physiology, Clin. J. Am. Soc. Nephrol. 3 (Supplement 3) (2008) S131–S139.
[20] S. Jin, F. Sun, Q. Zou, J. Huang, Y. Zuo, Y. Li, S. Wang, L. Cheng, Y. Man, F. Yang, Fish collagen and hydroxyapatite reinforced poly (lactide-co-glycolide) fibrous membrane for guided bone regeneration, Biomacromolecules 20 (5) (2019) 2058–2067.
[21] P. Deb, E. Barua, A.B. Deoghare, S.D. Lala, Development of bone scaffold using Puntius conchonius fish scale derived hydroxyapatite: physico-mechanical and bioactivity evaluations, Ceram. Int. 45 (8) (2019) 10004–10012.
[22] L. Liu, L. Zhang, B. Ren, F. Wang, Q. Zhang, Preparation and characterization of collagen–hydroxyapatite composite used for bone tissue engineering scaffold, Artif. Cells Blood Substit. Biotechnol. 31 (4) (2003) 435–448.
[23] H. Whiteman, Singapore frog farm reinvents Chinese elixir for modern times. https://edition.cnn.com/2015/10/26/asia/singapore-hashima-frog-farm/index.html, 2015. (Accessed 11 October 2019).
[24] W.F. Sheets, Fish farming and aquaculture. http://www.wildsingapore.com/wildfacts/concepts/aquaculture.htm, 2019. (Accessed 11 October 2019).
[25] H. Margolis, E. Moreno, Kinetics of hydroxyapatite dissolution in acetic, lactic, and phosphoric acid solutions, Calcif. Tissue Int. 50 (2) (1992) 137–143.
[26] Z. Xu, K.G. Neoh, A. Kishen, A biomimetic strategy to form calcium phosphate crystals on type I collagen substrate, Mater. Sci. Eng. C 30 (6) (2010) 822–826.
[27] J.K. Wang, G.M. Xiong, B. Luo, C.C. Choo, S. Yuan, N.S. Tan, C. Choong, Surface modification of PVDF using non-mammalian sources of collagen for enhancement of endothelial cell functionality, J. Mater. Sci. Mater. Med. 27 (3) (2016) 45.
[28] J.K. Wang, N.M.J. Cheam, S.A. Irvine, N.S. Tan, S. Venkatraman, C.Y. Tay, Interpenetrating network of alginate–human adipose extracellular matrix hydrogel for islet cells encapsulation, Macromol. Rapid Commun. 41 (21) (2020) 2000275.
[29] H. Yang, N.M.J. Cheam, H. Cao, M.K.H. Lee, S.K. Sze, N.S. Tan, C.Y. Tay, Materials stiffness-dependent redox metabolic reprogramming of mesenchymal stem cells for secretome-based therapeutic angiogenesis, Adv. Healthc. Mater. 8 (20) (2019), 1900929.
[30] J. Zhang, R. Duan, Characterisation of acid-soluble and pepsin-solubilised collagen from frog (Rana nigromaculata) skin, Int. J. Biol. Macromol. 101 (2017) 638–642.
[31] D. Coppola, M. Oliviero, G.A. Vitale, C. Lauritano, I. D'Ambra, S. Iannace, D. de Pascale, Marine collagen from alternative and sustainable sources: extraction, processing and applications, Mar. Drugs 18 (4) (2020) 214.
[32] Y. Zhao, Z. Wang, J. Zhang, T. Su, Extraction and characterization of collagen hydrolysates from the skin of Rana chensinensis, 3 Biotech 8 (3) (2018) 181.
[33] H. Li, B. Liu, L. Gao, H. Chen, Studies on bullfrog skin collagen, Food Chem. 84 (1) (2004) 65–69.
[34] B.D. Walters, J.P. Stegemann, Strategies for directing the structure and function of three-dimensional collagen biomaterials across length scales, Acta Biomater. 10 (4) (2014) 1488–1501.

[35] C.Y. Tay, M. Pal, H. Yu, W.S. Leong, N.S. Tan, K.W. Ng, S. Venkatraman, F. Boey, D. T. Leong, L.P. Tan, Bio-inspired micropatterned platform to steer stem cell differentiation, Small 7 (10) (2011) 1416–1421.
[36] C.Y. Tay, S.A. Irvine, F.Y. Boey, L.P. Tan, S. Venkatraman, Micro-/nano-engineered cellular responses for soft tissue engineering and biomedical applications, Small 7 (10) (2011) 1361–1378.
[37] J. Jeong, J.H. Kim, J.H. Shim, N.S. Hwang, C.Y. Heo, Bioactive calcium phosphate materials and applications in bone regeneration, Biomater. Res. 23 (1) (2019) 1–11.
[38] I. Zainon, N. Alwi, M. Abidin, H. Haniza, M. Ahmad, A. Ramli, Physicochemical properties of hydroxyapatite extracted from fish scales, Adv. Mat. Res. Trans. Tech. Publ. (2012) 235–239.
[39] C. Hallgren, H. Reimers, D. Chakarov, J. Gold, A. Wennerberg, An in vivo study of bone response to implants topographically modified by laser micromachining, Biomaterials 24 (5) (2003) 701–710.
[40] S. Yunoki, T. Suzuki, M. Takai, Stabilization of low denaturation temperature collagen from fish by physical cross-linking methods, J. Biosci. Bioeng. 96 (6) (2003) 575–577.
[41] C.M. Murphy, F.J. O'Brien, Understanding the effect of mean pore size on cell activity in collagen-glycosaminoglycan scaffolds, Cell Adhes. Migr. 4 (3) (2010) 377–381.
[42] M.B. Nair, A. Bernhardt, A. Lode, C. Heinemann, S. Thieme, T. Hanke, H. Varma, M. Gelinsky, A. John, A bioactive triphasic ceramic-coated hydroxyapatite promotes proliferation and osteogenic differentiation of human bone marrow stromal cells, J. Biomed. Mater. Res. A 90 (2) (2009) 533–542.
[43] A. Zareidoost, M. Yousefpour, B. Ghaseme, A. Amanzadeh, The relationship of surface roughness and cell response of chemical surface modification of titanium, J. Mater. Sci. Mater. Med. 23 (6) (2012) 1479–1488.
[44] H. Zheng, Y. Tian, Q. Gao, Y. Yu, X. Xia, Z. Feng, F. Dong, X. Wu, L. Sui, Hierarchical micro-nano topography promotes cell adhesion and osteogenic differentiation via integrin α2-PI3K-AKT signaling axis, Front. Bioeng. Biotechnol. 8 (2020) 463.
[45] Y. Xu, H. Li, J. Wu, Q. Yang, D. Jiang, B. Qiao, Polydopamine-induced hydroxyapatite coating facilitates hydroxyapatite/polyamide 66 implant osteogenesis: an in vitro and in vivo evaluation, Int. J. Nanomedicine 13 (2018) 8179.
[46] S.-W. Lee, M.-H. Lee, N. Oh, J.-A. Park, R. Leesungbok, S.-J. Ahn, Correlation between surface hydrophilicity and osteoblastic differentiation on microgrooved titanium substrata, J. Oral Implantol. 38 (1) (2012) 11–19.
[47] A. Autissier, C. Le Visage, C. Pouzet, F. Chaubet, D. Letourneur, Fabrication of porous polysaccharide-based scaffolds using a combined freeze-drying/cross-linking process, Acta Biomater. 6 (9) (2010) 3640–3648.
[48] J. Chen, J. Irianto, S. Inamdar, P. Pravincumar, D. Lee, D.L. Bader, M. Knight, Cell mechanics, structure, and function are regulated by the stiffness of the three-dimensional microenvironment, Biophys. J. 103 (6) (2012) 1188–1197.
[49] N. Huebsch, P.R. Arany, A.S. Mao, D. Shvartsman, O.A. Ali, S.A. Bencherif, J. Rivera-Feliciano, D.J. Mooney, Harnessing traction-mediated manipulation of the cell/matrix interface to control stem-cell fate, Nat. Mater. 9 (6) (2010) 518–526.
[50] K. Vuornos, H. Huhtala, M. Kääriäinen, K. Kuismanen, L. Hupa, M. Kellomäki, S. Miettinen, Bioactive glass ions for in vitro osteogenesis and microvascularization in gellan gum-collagen hydrogels, J Biomed Mater Res B Appl Biomater 108 (4) (2020) 1332–1342.
[51] A.J. Ryan, J.P. Gleeson, A. Matsiko, E.M. Thompson, F.J. O'Brien, Effect of different hydroxyapatite incorporation methods on the structural and biological properties of porous collagen scaffolds for bone repair, J. Anat. 227 (6) (2015) 732–745.
[52] J. Chen, M. Birch, S. Bull, Nanomechanical characterization of tissue engineered bone grown on titanium alloy in vitro, J. Mater. Sci. Mater. Med. 21 (1) (2010) 277–282.
[53] D. Paramitha, M. Ulum, A. Purnama, D. Wicaksono, D. Noviana, H. Hermawan, Monitoring degradation products and metal ions in vivo, in: Monitoring and Evaluation of Biomaterials and Their Performance In Vivo, Elsevier, 2017, pp. 19–44.
[54] P. Kazimierczak, A. Benko, M. Nocun, A. Przekora, Novel chitosan/agarose/hydroxyapatite nanocomposite scaffold for bone tissue engineering applications: comprehensive evaluation of biocompatibility and osteoinductivity with the use of osteoblasts and mesenchymal stem cells, Int. J. Nanomedicine 14 (2019) 6615.
[55] C.Y. Tay, C.G. Koh, N.S. Tan, D.T. Leong, L.P. Tan, Mechanoregulation of stem cell fate via micro-/nano-scale manipulation for regenerative medicine, Nanomedicine 8 (4) (2013) 623–638.
[56] M. Mizerska-Kowalska, A. Sławińska-Brych, K. Kałwaj, A. Żurek, B. Pawińska, W. Rzeski, B. Zdzisińska, Betulin promotes differentiation of human osteoblasts in vitro and exerts an osteoinductive effect on the hFOB 1.19 cell line through activation of JNK, ERK1/2, and mTOR kinases, Molecules 24 (14) (2019) 2637.
[57] A. Rutkovskiy, K.-O. Stensløkken, I.J. Vaage, Osteoblast differentiation at a glance, Med. Sci. Monit. Basic Res. 22 (2016) 95.
[58] J. Venugopal, S. Low, A.T. Choon, T.S. Kumar, S. Ramakrishna, Mineralization of osteoblasts with electrospun collagen/hydroxyapatite nanofibers, J. Mater. Sci. Mater. Med. 19 (5) (2008) 2039–2046.
[59] L. Chen, Z. Wu, Y. Zhou, L. Li, Y. Wang, Z. Wang, Y. Chen, P. Zhang, Biomimetic porous collagen/hydroxyapatite scaffold for bone tissue engineering, J. Appl. Polym. Sci. 134 (37) (2017) 45271.
[60] P. Duan, R. Toumpaniari, S. Partridge, M.A. Birch, P.G. Genever, S.J. Bull, K. W. Dalgarno, A.W. McCaskie, J. Chen, How cell culture conditions affect the microstructure and nanomechanical properties of extracellular matrix formed by immortalized human mesenchymal stem cells: an experimental and modelling study, Mater. Sci. Eng. C 89 (2018) 149–159.